Chapter 6
Simulating anisotropic diffusion in heterogeneous brain regions

In this chapter, we return to our model problem (1.1) and bring together the different tools and techniques introduced in Chapters 3 to 5. The computational domain will be determined from T1-weighted data and divided into grey and white matter subdomains, diffusion tensor imaging (DTI) data will be employed in the construction of the heterogeneous and anisotropic diffusion tensor, and specific sub regions, such as the hippocampus, will be selected to assess site-specific clearance.

In practice, one should first address data and mesh resolution issues. For instance, raw DTI data can exhibit rough transitions, as well as noise. This is particularly true in the grey matter proximal to cerebrospinal fluid (e.g. Figures 5.2 and 5.4 in Chapter 5). Here, we assume that the DTI data have been suitably smoothened and denoised for use in simulations. In addition, we must ascertain a mesh resolution that is suitable to provide reliable estimates of the spread and clearance of different molecules, while avoiding the unnecessary computational costs associated with over-resolving the mesh.

6.1 Molecular diffusion in one dimension

To estimate the required spatial mesh resolution, the discrete time step, and the time scale of solute clearance, it is useful to first consider equation (1.1) in one dimension for different molecules. Here, we consider the protein fragment amyloid-beta (Aβ) associated with neurodegenerative disease [31], the tracer gadobutrol used in glymphatic magnetic resonance imaging [52], and water.

The effective diffusion coefficient D in brain tissue for each of these molecules is estimated to be 6.2×10^{-5} mm^2/s, 1.3×10^{-4} mm^2/s, and 1.1×10^{-3} mm^2/s, respectively [65, 63].

6.1.1 Analytical solution

In one dimension and over the domain $(0,\infty)$, the parabolic diffusion problem (1.1) with $u_0(x)=0$, $u(0,t)=1$, and $u(\infty,t)=0$ allows for a simple analytic solution:

$$u(x,t)=\operatorname{erfc}(x/(2\sqrt{Dt})). \tag{6.1}$$

Figure 6.1 shows solutions of (6.1) zoomed in on the (left) first 2 mm of the domain, and the (middle) first 10 mm after 9 hours, and (right) the first 10 mm after 24 hours. It is evident that diffusion is a slow process: significant concentration changes occur within 2 mm of the boundary after 9 hours; however, 1 cm away, the heavier molecules, amyloid-beta and gadobutrol, still have concentrations near zero. The source code for generating these plots is available in `mri2fem/chp6/analytical_1D.py`.

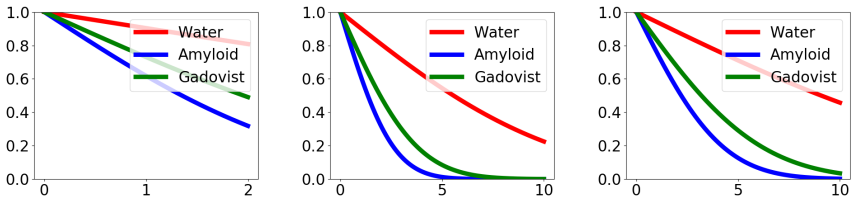

Fig. 6.1 Diffusion according to (6.1): concentration (y-axis, arbitrary unit) versus distance from the source/left boundary (x-axis, in mm) after 9 hours (left and middle) and after 24 hours (right).

6.1.2 Numerical solution and handling numerical artifacts

We next discretize (1.1) using the finite element method (as described in Chapter 3). Note, however, that the sharp change in the boundary versus initial

conditions for our model problem can lead to artificial oscillations in the numerical solution. Such oscillations often diminish with refinement; they can also be avoided through the use of monotonic or maximum principle preserving schemes. Another common method, which we consider here, for Galerkin finite element schemes is mass lumping (e.g. [39]). We provide FEniCS-based source code for the finite element solution of (1.1) with and without mass lumping in `mri2fem/chp6/diffusion_1D.py`. To use this script, see, for example

```
$ cd mri2fem/chp6
$ python3 diffusion_1D.py --help
```

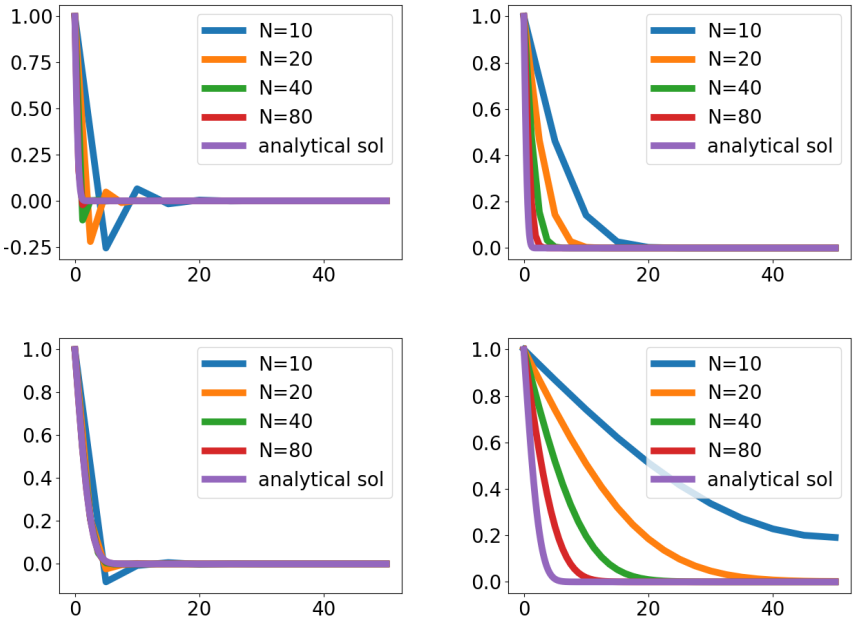

Fig. 6.2 Comparison of standard Galerkin (left) and mass-lumped (right) finite element schemes of the diffusion equation (1.1) in one dimension over $\Omega = (0, 50)$ mm. The amyloid-beta concentration (y-axis, arbitrary unit) versus length (x-axis, in mm). Upper row: solution at time $t = 30$ minutes, with $\Delta t = 5$ minutes. Lower row: Solution at time $t = 9$ hours.

The standard and mass-lumped finite element solutions are shown in Figure 6.2 at different times and with different time steps. Early, for coarse resolutions ($N = 10$ or $N = 20$), the standard approach yields considerable nonphysical oscillations, whereas the mass-lumped solution (right) produces significant numerical diffusion. However, in the longer term context, the standard Galerkin scheme is clearly desirable: the former allows for a spatial resolution of $N = 10$ or $N = 20$, whereas the latter requires $N = 40$ or $N = 80$ to control the numerical diffusion. Essentially, the initial error from the short-term Gibbs phenomena, that is, the discontinuous initial data, is no match for the long-term regularizing effect of the parabolic partial differential equation. Therefore, these early errors do not contribute much to the long-term numerical solution.

In conclusion, these results suggest that, if we are interested in long-term dynamics, a time step size of $\Delta t \approx 5$ minutes with a spatial resolution of $N = 10$ or $N = 20$, corresponding roughly to a quasi-uniform mesh cell diameter of $0.25 \text{ mm} \leq h \leq 0.5 \text{ mm}$, is a good starting target for the standard Galerkin approach in our three dimensional (3D) discretization. Conversely, a mesh size of $N = 80$, or $h \approx 6.25 \times 10^{-2}$ mm, is needed for the mass-lumped case. This would be a much more costly choice on a 3D mesh, and unnecessary if the short-term dynamics need not be resolved.

6.2 Anisotropic diffusion in 3D brain regions

In this section, we consider simulations of gadobutrol diffusion and compute the average concentrations in different brain regions. In particular, we begin with the following steps:

- We create a brain mesh with grey and white matter marked and ventricles removed and mark parcellation regions as described in Chapter 4.4.2.
- We filter and map our DTI data onto this geometry as described in Chapter 5.2.2.
- Using FEniCS, we implement a version of the diffusion simulation script presented in Chapter 3.3.3 allowing for anisotropic diffusion and the computation of integrals over labelled regions.

In the numerical simulation, we represent the DTI data in the form of a heterogeneous and anisotropic diffusion tensor field D. The FEniCS code for setting up the diffusion tensor field reads

```
# read the DTI
T = TensorFunctionSpace(mesh, "DG", 0)
D = Function(T)
hdf.read(D, "/DTI")
```

We compute the average amount of tracer in a labelled region by integrating the concentration over the region and dividing by the region's volume as follows (with the regions labelled 17 and 1035 as examples):

```
    unit17 += [assemble(u*dx(17))/vol17]
    unit1035 += [assemble(u*dx(1035))/vol1035]
```

The precise commands run are included in `mri2fem/chp6/all.sh`, and the script `mri2fem/chp6/chp6-diffusion-mritracer.py` gives the complete FEniCS code.

6.2.1 Regional distribution of gadobutrol

We compute the average concentrations of gadobutrol diffusing in from the brain's surface in regions 17 (hippocampus), 1035 (insula grey matter), 3035 (insula white matter), 1028 (superior frontal grey matter), and 3028 (superior frontal white matter). Gadobutrol has a diffusivity approximately twice that of amyloid-beta, and the estimated mesh size and time step of the previous section should therefore apply to this case as well. The resulting curves are shown in Figure 6.3, and the simulations are shown in Figures 6.4–6.5. Note that, here, we consider the tracer distribution in certain regions as a function of time; the distribution therefore starts at a low value and increases with time as the solute diffuses throughout the brain. Clearly, the distribution of gadobutrol in the grey matter regions and hippocampus are affected much more than in the white matter regions. This result is expected since both the grey matter and hippocampus are closer to the cerebrospinal fluid where, in our simulation, the gadobutrol concentration is assumed to reside initially. It is also observed that the upper regions, that is, the superior frontal grey and white matter (1028 and 3028, respectively), experience faster gadobutrol deposition than the corresponding regions on the side of the brain.

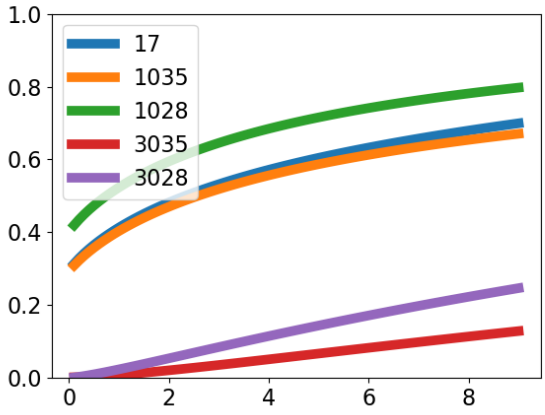

Fig. 6.3 Average concentration of gadobutrol (y-axis, arbitrary unit) versus time (x-axis, hours) in different brain regions: 17 (hippocampus), 1035 (insula grey matter), 3035 (insula white matter), 1028 (superior frontal grey matter), and 3028 (superior frontal white matter). Time step: 6 minutes, $N = 64$ brain mesh (cf. below).

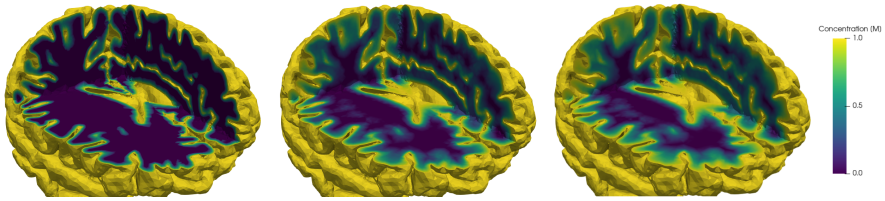

Fig. 6.4 The simulated distribution of gadobutrol, for a mesh with resolution parameter set to 32, after 0 hours (left), after 5 hours (middle) and after 9 hours (right).

6.2.2 Accuracy and convergence of computed quantities

A common question and topic in numerical simulations is whether the computed solutions have converged. We therefore investigate next the mesh convergence of the standard Galerkin and mass-lumped Galerkin approaches. More precisely, we consider a set of meshes, aiming to determine the accuracy of the numerical solution. In this example, we consider a roughly uniform refinement, but the mesh is not refined in place; rather, a sequence of meshes is first generated at different resolutions using the surface volume meshing toolkit

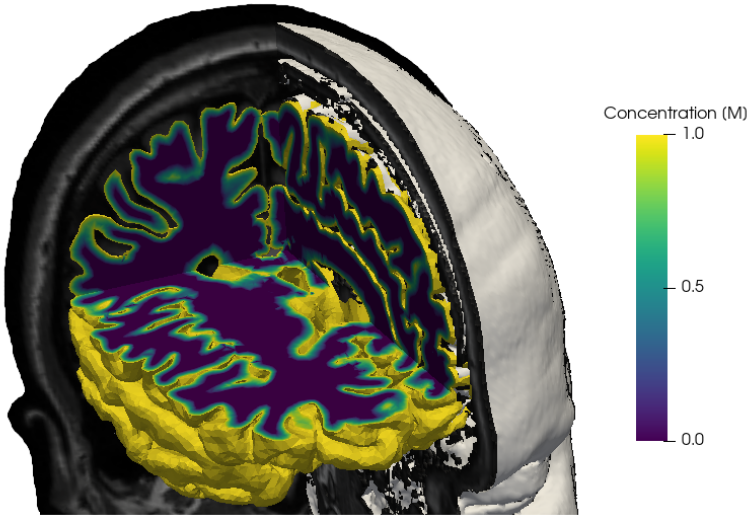

Fig. 6.5 Illustration of the simulated distribution of solute concentration in the brain within the cranium.

(SVM-Tk). In particular, we construct a sequence of quasi-uniform meshes, as follows (using `mri2fem/chp6/create_mesh_refinements.py`):

```
import SVMTK as svmtk
import time

# Import surfaces, and merge lh/rh white surfaces
ventricles  = svmtk.Surface("surfaces/lh.ventricles.stl")
lhpial = svmtk.Surface("surfaces/lh.pial.stl")
rhpial = svmtk.Surface("surfaces/rh.pial.stl")
white = svmtk.Surface("surfaces/lh.white.stl")
rhwhite = svmtk.Surface("surfaces/rh.white.stl")
white.union(rhwhite)

surfaces = [lhpial, rhpial, white, ventricles]

# Create subdomain map
smap = svmtk.SubdomainMap()
smap.add("1000", 1)
smap.add("0100", 1)
smap.add("0110", 2)
smap.add("0010", 2)
smap.add("1010", 2)
```

```
smap.add("0111", 3)
smap.add("1011", 3)

# Create domain
domain = svmtk.Domain(surfaces, smap)

# Create meshes of increasing resolutions
Ns = [16, 32, 64, 128]
for N in Ns:
    print("Creating mesh for N=%d" % N)
    t0 = time.time()
    domain.create_mesh(N)
    domain.remove_subdomain([3])
    domain.save("brain_%d.mesh" % N)
    t1 = time.time()
    print("Done! That took %g sec" % (t1-t0))
```

After creating the meshes we mark the subdomains of interest and map the DTI data onto the mesh, before running the simulations. The following is a code snippet from `mri2fem/chp6/all.sh` that shows how the 16 mesh is created by the scripts described in the previous chapters:

```
# using the 16 mesh
# convert to h5
python3 ../chp4/convert_to_dolfin_mesh.py \
   --meshfile brain_16.mesh --hdf5file brain_16.h5

# mark subdomains
python3 ../chp4/add_parcellations.py \
    --in_hdf5 brain_16.h5 \
   --in_parc ../chp4/wmparc.mgz \
   --out_hdf5 brain_16_tags.h5 \
   --add 17 1028 1035 3028 3035

# add dti to the h5 file
python3 ../chp5/dti_data_to_mesh.py  \
   --dti ../chp5/clean-dti.mgz \
   --mesh brain_16_tags.h5 --label 1 0.4 0.6 \
   --out DTI_16.h5

# run simulation
python3 chp6-diffusion-mritracer.py --mesh DTI_16.h5 \
   --lumped lumped --label uniform16lumped
```

```
python3 chp6-diffusion-mritracer.py --mesh DTI_16.h5 \
   --lumped not --label uniform16notlumped
```

The average gadobutrol concentrations in the hippocampus over time for the sequence of meshes generated here are shown in Figure 6.6, with (right) and without (left) mass lumping. Clearly, the standard Galerkin approach (left) seems to yield more consistent results than the mass-lumped Galerkin scheme (right). However, even for the standard Galerkin scheme, whether the solutions are fully converged seems questionable at the highest resolution tested (around 15.5 million mesh cells). Recall that piecewise constants are used to represent the anisotropic diffusion tensor D. This DG construction requires about nine entries per cell, thus yielding approximately 140 million values for 15.5 million cells. Higher resolutions, such as those for piecewise linear or quadratic constructions, are not feasible on a personal computing device with only 32 gigabytes of RAM.

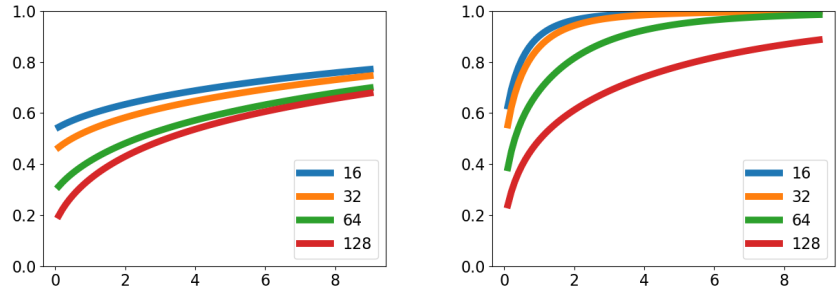

Fig. 6.6 Average gadobutrol concentration in the hippocampus (y-axis, arbitrary unit) versus time (x-axis, hours) for different mesh resolutions, $\Delta t = 6$ min. Quasi-uniform mesh sequence with $N = 16$, 32, 64, 128 generated by SVM-Tk. Standard Galerkin (left) versus mass-lumped Galerkin (right) discretizations.

To further assess the accuracy and convergence of the computed concentrations under mesh refinements, we therefore also consider adaptively refined meshes. In particular, we focus on the hippocampus and adaptively refine the meshes in this region, starting from the $N = 16$ brain mesh of the previous mesh sequence. Again, we plot the average gadobutrol concentrations in the hippocampus over time for a sequence of adaptively refined meshes (see Figure 6.7 with (right) and without (left) mass-lumping). Using this technique,

we find the solutions between the second, third, and fourth adaptive refinements differ little for the standard scheme. However, mesh convergence for the mass-lumped Galerkin strategy remains unclear, even after four refinements to the hippocampal region. Finally, looking at the mesh statistics (number of vertices, cells, and range of mesh sizes) for the uniformly and adaptively refined meshes (Tables 6.2.2 and 6.2.2), we note that the actual h required for mesh convergence is around two to ten times smaller than our initial estimate (Section 6.1).

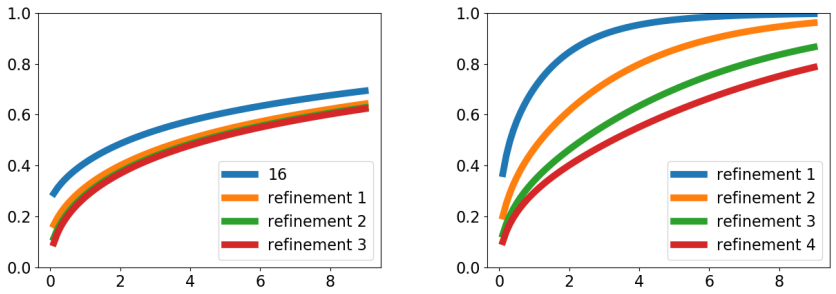

Fig. 6.7 Average gadobutrol concentration in the hippocampus (y-axis, arbitrary unit) versus time (x-axis, hours) for a sequence of adaptively refined meshes, $\Delta t = 6$ minutes. Standard Galerkin (left) versus mass-lumped Galerkin (right) discretizations.

Refinement	Vertices	Cells	$h_{\min}$	$h_{\max}$
16	94K	457K	0.97	11.4
32	194K	908K	0.46	5.7
64	567K	2.75M	0.26	2.9
128	2.8M	15.5M	0.14	1.45

Refinement	Vertices	Cells	$h_{\min}$	$h_{\max}$
1	99K	479K	0.64	11.4
2	123K	613K	0.30	11.4
3	275K	1.5M	0.14	11.4
4	1.3M	7.7M	0.07	11.4

Table 6.1 Mesh statistics (number of vertices, cells, and minimal and maximal cell sizes) for the (left) uniformly refined and (right) adaptively refined mesh sequences.

Index

References

1. *FEniCS Project*, 2020, https://fenicsproject.org.
2. *FreeSurfer*, 2020, https://surfer.nmr.mgh.harvard.edu/.
3. *FreeSurfer Wiki*, 2020, https://surfer.nmr.mgh.harvard.edu/fswiki.
4. *Paraview*, 2020, https://www.paraview.org.
5. N. J. Abbott, M. E. Pizzo, J. E. Preston, D. Janigro, and R. G. Thorne, *The role of brain barriers in fluid movement in the CNS: is there a "glymphatic" system?*, Acta neuropathologica, 135 (2018), pp. 387–407.
6. J. Ahrens, B. Geveci, and C. Law, *Paraview: An end-user tool for large data visualization*, The visualization handbook, 717 (2005).
7. R. Aldea, R. O. Weller, D. M. Wilcock, R. O. Carare, and G. Richardson, *Cerebrovascular smooth muscle cells as the drivers of intramural periarterial drainage of the brain*, Frontiers in aging neuroscience, 11 (2019), p. 1.
8. A. L. Alexander, J. E. Lee, M. Lazar, and A. S. Field, *Diffusion tensor imaging of the brain*, Neurotherapeutics, 4 (2007), pp. 316–329.
9. M. Alnæs, J. Blechta, J. Hake, A. Johansson, B. Kehlet, A. Logg, C. Richardson, J. Ring, M. E. Rognes, and G. N. Wells, *The FEniCS project version 1.5*, Archive of Numerical Software, 3 (2015).
10. N. Alperin and A. M. Bagci, *Spaceflight-induced visual impairment and globe deformations in astronauts are linked to orbital cerebrospinal fluid volume increase*, in Intracranial Pressure & Neuromonitoring XVI, Springer, 2018, pp. 215–219.
11. K. Archie, *Dicombrowser*, 2020, https://nrg.wustl.edu/software/dicom-browser/.
12. W. F. Boron and E. L. Boulpaep, *Medical Physiology*, Elsevier Health Sciences, 2016.
13. M. Brett et al., *nipy/nibabel: 3.2.1*, Nov. 2020, https://doi.org/10.5281/zenodo.4295521.
14. S. Budday, T. C. Ovaert, G. A. Holzapfel, P. Steinmann, and E. Kuhl, *Fifty shades of brain: a review on the mechanical testing and modeling of brain tissue*, Archives of Computational Methods in Engineering, (2019), pp. 1–44.
15. D. Chou, J. C. Vardakis, L. Guo, B. J. Tully, and Y. Ventikos, *A fully dynamic multi-compartmental poroelastic system: Application to aqueductal stenosis*, Journal of biomechanics, 49 (2016), pp. 2306–2312.

16. M. Croci, V. Vinje, and M. E. Rognes, *Uncertainty quantification of parenchymal tracer distribution using random diffusion and convective velocity fields*, Fluids and Barriers of the CNS, 16 (2019), p. 32.
17. A. M. Dale, B. Fischl, and M. I. Sereno, *Cortical surface-based analysis: I. segmentation and surface reconstruction*, Neuroimage, 9 (1999), pp. 179–194.
18. C. Daversin-Catty, V. Vinje, K.-A. Mardal, and M. E. Rognes, *The mechanisms behind perivascular fluid flow*, Plos one, 15 (2020), p. e0244442.
19. A. K. Diem, M. MacGregor Sharp, M. Gatherer, N. W. Bressloff, R. O. Carare, and G. Richardson, *Arterial pulsations cannot drive intramural periarterial drainage: significance for Aβ drainage*, Frontiers in neuroscience, 11 (2017), p. 475.
20. A. Fabri, G.-J. Giezeman, L. Kettner, S. Schirra, and S. Schönherr, *On the design of CGAL, a computational geometry algorithms library*, Software: Practice and Experience, 30 (2000), pp. 1167–1202.
21. S. Fornari, A. Schäfer, M. Jucker, A. Goriely, and E. Kuhl, *Prion-like spreading of alzheimer's disease within the brain's connectome*, Journal of the Royal Society Interface, 16 (2019), p. 20190356.
22. C. Geuzaine and J.-F. Remacle, *Gmsh: A 3-d finite element mesh generator with built-in pre-and post-processing facilities*, International journal for numerical methods in engineering, 79 (2009), pp. 1309–1331.
23. M. S. Gockenbach, *Understanding and implementing the finite element method*, vol. 97, SIAM, 2006.
24. A. Goriely, M. G. Geers, G. A. Holzapfel, J. Jayamohan, A. Jérusalem, S. Sivaloganathan, W. Squier, J. A. van Dommelen, S. Waters, and E. Kuhl, *Mechanics of the brain: perspectives, challenges, and opportunities*, Biomechanics and modeling in mechanobiology, 14 (2015), pp. 931–965.
25. H. Gray, *Gray's anatomy: with original illustrations by Henry Carter*, Arcturus Publishing, 2009.
26. R. Grech, T. Cassar, J. Muscat, K. P. Camilleri, S. G. Fabri, M. Zervakis, P. Xanthopoulos, V. Sakkalis, and B. Vanrumste, *Review on solving the inverse problem in EEG source analysis*, Journal of neuroengineering and rehabilitation, 5 (2008), p. 25.
27. E. M. Haacke, R. W. Brown, M. R. Thompson, R. Venkatesan, M. Thompson, M. Venkatesan, M. Haacke, W. Brown, and M. Thompson, *Magnetic resonance imaging: physical principles and sequence design*, (1999).
28. P. T. Haga, G. Pizzichelli, M. Mortensen, M. Kuchta, S. H. Pahlavian, E. Sinibaldi, B. A. Martin, and K.-A. Mardal, *A numerical investigation of intrathecal isobaric drug dispersion within the cervical subarachnoid space*, PloS one, 12 (2017), p. e0173680.
29. K. E. Holter, B. Kehlet, A. Devor, T. J. Sejnowski, A. M. Dale, S. W. Omholt, O. P. Ottersen, E. A. Nagelhus, K.-A. Mardal, and K. H. Pettersen, *Interstitial solute transport in 3D reconstructed neuropil occurs by diffusion rather than bulk flow*, Proceedings of the National Academy of Sciences, 114 (2017), pp. 9894–9899.
30. J. D. Hunter, *Matplotlib: A 2D graphics environment*, Computing in science & engineering, 9 (2007), pp. 90–95.
31. J. J. Iliff, M. Wang, Y. Liao, B. A. Plogg, W. Peng, G. A. Gundersen, H. Benveniste, G. E. Vates, R. Deane, S. A. Goldman, et al., *A paravascular*

pathway facilitates CSF flow through the brain parenchyma and the clearance of interstitial solutes, including amyloid β, Science translational medicine, 4 (2012), pp. 147ra111–147ra111.
32. J. J. Iliff, M. Wang, D. M. Zeppenfeld, A. Venkataraman, B. A. Plog, Y. Liao, R. Deane, and M. Nedergaard, *Cerebral arterial pulsation drives paravascular CSF–interstitial fluid exchange in the murine brain*, Journal of Neuroscience, 33 (2013), pp. 18190–18199.
33. M. Jenkinson, C. F. Beckmann, T. E. Behrens, M. W. Woolrich, and S. M. Smith, *FSL*, Neuroimage, 62 (2012), pp. 782–790.
34. N. A. Jessen, A. S. F. Munk, I. Lundgaard, and M. Nedergaard, *The glymphatic system: a beginner's guide*, Neurochemical research, 40 (2015), pp. 2583–2599.
35. B. Jeurissen, M. Descoteaux, S. Mori, and A. Leemans, *Diffusion MRI fiber tractography of the brain*, NMR Biomed., 32 (2017), p. e3785, https://doi.org/doi.org/10.1002/nbm.3785.
36. P. Kevrekidis, T. B. Thompson, and A. Goriely, *Anisotropic diffusion and traveling waves of toxic proteins in neurodegenerative diseases*, Physics Letters A, 384 (2020), p. 126935.
37. G. Kindlmann, R. S. J. Estepar, M. Niethammer, S. Haker, and C.-F. Westin, *Geodesic-loxodromes for diffusion tensor interpolation and difference measurement*, in International Conference on Medical Image Computing and Computer-Assisted Intervention, Springer, 2007, pp. 1–9.
38. P. Kochunov, D. C. Glahn, J. Lancaster, P. M. Thompson, V. Kochunov, B. Rogers, P. Fox, J. Blangero, and D. Williamson, *Fractional anisotropy of cerebral white matter and thickness of cortical gray matter across the lifespan*, Neuroimage, 58 (2011), pp. 41–49.
39. H. P. Langtangen and A. Logg, *Solving PDEs in Python: The FEniCS Tutorial I*, vol. 1, Springer, 2016.
40. H. P. Langtangen and K.-A. Mardal, *Introduction to numerical methods for variational problems*, vol. 21, Springer Nature, 2019.
41. J. J. Lee, E. Piersanti, K.-A. Mardal, and M. E. Rognes, *A mixed finite element method for nearly incompressible multiple-network poroelasticity*, SIAM Journal on Scientific Computing, 41 (2019), pp. A722–A747.
42. A. Logg, K.-A. Mardal, and G. Wells, *Automated solution of differential equations by the finite element method: The FEniCS book*, vol. 84, Springer Science & Business Media, 2012.
43. K.-A. Mardal, M. E. Rognes, T. B. Thompson, and L. M. Valnes, *mri2fem data set*, Dec. 2020, https://doi.org/10.5281/zenodo.4386987.
44. K.-A. Mardal, M. E. Rognes, T. B. Thompson, and L. M. Valnes, *Software for Mathematical modeling of the human brain – from magnetic resonance images to finite element simulation*, Dec. 2020, https://doi.org/10.5281/zenodo.4386999.
45. A. Meurer, C. P. Smith, M. Paprocki, O. Čertík, S. B. Kirpichev, M. Rocklin, A. Kumar, S. Ivanov, J. K. Moore, S. Singh, et al., *SymPy: symbolic computing in Python*, PeerJ Computer Science, 3 (2017), p. e103.
46. P. Mildenberger, M. Eichelberg, and E. Martin, *Introduction to the DICOM standard*, European radiology, 12 (2002), pp. 920–927.
47. O. Naggara, C. Oppenheim, D. Rieu, N. Raoux, S. Rodrigo, G. Dalla Barba, and J.-F. Meder, *Diffusion tensor imaging in early Alzheimer's disease*, Psychiatry Research: Neuroimaging, 146 (2006), pp. 243–249.

48. S. J. Payne, *Cerebral Blood Flow and Metabolism: A Quantitative Approach*, World Scientific, 2017.
49. G. Pizzichelli, B. Kehlet, Ø. Evju, B. Martin, M. Rognes, K. Mardal, and E. Sinibaldi, *Numerical study of intrathecal drug delivery to a permeable spinal cord: effect of catheter position and angle*, Computer Methods in Biomechanics and Biomedical Engineering, 20 (2017), pp. 1599–1608.
50. R. A. Pooley, *Fundamental physics of mr imaging*, Radiographics, 25 (2005), pp. 1087–1099.
51. L. Ray, J. J. Iliff, and J. J. Heys, *Analysis of convective and diffusive transport in the brain interstitium*, Fluids and Barriers of the CNS, 16 (2019), p. 6.
52. G. Ringstad, L. M. Valnes, A. M. Dale, A. H. Pripp, S.-A. S. Vatnehol, K. E. Emblem, K.-A. Mardal, and P. K. Eide, *Brain-wide glymphatic enhancement and clearance in humans assessed with MRI*, JCI insight, 3 (2018).
53. L. Roscoe et al., *Stereolithography interface specification*, America-3D Systems Inc, 27 (1988), p. 10.
54. N. Schlömer, G. McBain, T. Li, V. M. Ferrándiz, eolianoe, L. Dalcin, K. Luu, nilswagner, A. Gupta, S. Müller, L. Schwarz, J. Blechta, C. Coutinho, D. Beurle, B. Shrimali, A. Cervone, Nate, U. Mishra, T. Heister, T. Langlois, S. Peak, S. Sharma, M. Bussonnier, lgiraldi, G. Jacquenot, G. A. Vaillant, C. Wilson, A. U. Gudchenko, and A. Croucher, *nschloe/meshio 3.2.14*, Nov. 2019, https://doi.org/10.5281/zenodo.3548723.
55. W. B. Scoville and B. Milner, *Loss of recent memory after bilateral hippocampal lesions*, Journal of neurology, neurosurgery, and psychiatry, 20 (1957), p. 11.
56. M. K. Sharp, R. O. Carare, and B. A. Martin, *Dispersion in porous media in oscillatory flow between flat plates: applications to intrathecal, periarterial and paraarterial solute transport in the central nervous system*, Fluids and Barriers of the CNS, 16 (2019), p. 13.
57. A. J. Smith, X. Yao, J. A. Dix, B.-J. Jin, and A. S. Verkman, *Test of the "glymphatic" hypothesis demonstrates diffusive and aquaporin-4-independent solute transport in rodent brain parenchyma*, Elife, 6 (2017), p. e27679.
58. J. Soares, P. Marques, V. Alves, and N. Sousa, *A hitchhiker's guide to diffusion tensor imaging*, Frontiers in neuroscience, 7 (2013), p. 31.
59. L. R. Squire, *The legacy of patient HM for neuroscience*, Neuron, 61 (2009), pp. 6–9.
60. E. Syková and C. Nicholson, *Diffusion in brain extracellular space*, Physiological reviews, 88 (2008), pp. 1277–1340.
61. G. Taubin, *Curve and surface smoothing without shrinkage*, in Proceedings of IEEE international conference on computer vision, IEEE, 1995, pp. 852–857.
62. A. Tveito and R. Winther, *Introduction to partial differential equations: a computational approach*, vol. 29, Springer Science & Business Media, 2004.
63. L. M. Valnes, S. K. Mitusch, G. Ringstad, P. K. Eide, S. W. Funke, and K.-A. Mardal, *Apparent diffusion coefficient estimates based on 24 hours tracer movement support glymphatic transport in human cerebral cortex*, Scientific Reports, 10 (2020), pp. 1–12.
64. I. Voldsbekk, I. I. Maximov, N. Zak, D. Roelfs, O. Geier, P. Due-Tønnessen, T. Elvsåshagen, M. Strømstad, A. Bjørnerud, and I. Groote, *Evidence for wakefulness-related changes to extracellular space in human brain white matter from diffusion-weighted MRI*, NeuroImage, (2020), p. 116682.

65. J. Waters, *The concentration of soluble extracellular amyloid-β protein in acute brain slices from crnd8 mice*, PLoS One, 5 (2010), p. e15709.
66. L. Xie, H. Kang, Q. Xu, M. J. Chen, Y. Liao, M. Thiyagarajan, J. O'Donnell, D. J. Christensen, C. Nicholson, J. J. Iliff, et al., *Sleep drives metabolite clearance from the adult brain*, science, 342 (2013), pp. 373–377.